

# Terahertz transmission vs reflection imaging and model-based characterization for excised breast carcinomas

TYLER BOWMAN,<sup>1,\*</sup> MAGDA EL-SHENAWEI,<sup>1</sup> AND LUCAS K. CAMPBELL<sup>2</sup>

<sup>1</sup>Department of Electrical Engineering, University of Arkansas, 3217 Bell Engineering Center, Fayetteville, AR 72701, USA

<sup>2</sup>Northwest Arkansas Pathology Associates, P. A., 390 E. Longview St. Fayetteville, AR 72703, USA  
\*[tcbowman@uark.edu](mailto:tcbowman@uark.edu)

**Abstract:** This work presents experimental and analytical comparison of terahertz transmission and reflection imaging modes for assessing breast carcinoma in excised paraffin-embedded human breast tissue. Modeling for both transmission and reflection imaging is developed. The refractive index and absorption coefficient of the tissue samples are obtained. The reflection measurements taken at the system's fixed oblique angle of 30° are shown to be a hybridization of *TE* and *TM* modes. The models are validated with transmission spectroscopy at fixed points on fresh bovine muscle and fat tissues. Images based on the calculated absorption coefficient and index of refraction of bovine tissue are successfully compared with the terahertz magnitude and phase measured in the reflection mode. The validated techniques are extended to 20 and 30 μm slices of fixed human lobular carcinoma and infiltrating ductal carcinoma mounted on polystyrene microscope slides in order to investigate the terahertz differentiation of the carcinoma with non-cancerous tissue. Both transmission and reflection imaging show clear differentiation in carcinoma versus healthy tissue. However, when using the reflection mode, in the calculation of the thin tissue properties, the absorption is shown to be sensitive to small phase variations that arise due to deviations in slide and tissue thickness and non-ideal tissue adhesion. On the other hand, the results show that the transmission mode is much less sensitive to these phase variations. The results also demonstrate that reflection imaging provides higher resolution and more clear margins between cancerous and fibroglandular regions, cancerous and fatty regions, and fibroglandular and fatty tissue regions. In addition, more features consistent with high power pathology images are exhibited in the reflection mode images.

©2016 Optical Society of America

**OCIS codes:** (170.6795) Terahertz imaging; (170.6935) Tissue characterization; (300.6495) Spectroscopy, terahertz.

## References and links

1. P. U. Jepsen, D. G. Cooke, and M. Koch, "Terahertz spectroscopy and imaging - Modern techniques and applications," *Laser Photonics Rev.* **5**(1), 124–166 (2011).
2. Y. C. Shen, T. Lo, P. F. Taday, B. E. Cole, W. R. Tribe, and M. C. Kemp, "Detection and identification of explosives using terahertz pulsed spectroscopic imaging," *Appl. Phys. Lett.* **86**(24), 241116 (2005).
3. R. Ulbricht, E. Hendry, J. Shan, T. F. Heinz, and M. Bonn, "Carrier dynamics in semiconductors studied with time-resolved terahertz spectroscopy," *Rev. Mod. Phys.* **83**(2), 543–586 (2011).
4. N. M. Burford, M. El-Shenawee, C. B. O'Neal, and K. J. Olejniczak, "Terahertz Imaging for Nondestructive Evaluation of Packaged Power Electronic Devices," *Int. J. Emerg. Technol. Adv. Eng.* **4**, 395–401 (2014).
5. S. Fan, Y. He, B. S. Ung, and E. Pickwell-MacPherson, "The growth of biomedical terahertz research," *J. Phys. D Appl. Phys.* **47**(37), 374009 (2014).
6. P. H. Siegel, "Terahertz technology in biology and medicine," *IEEE Trans. Microw. Theory Tech.* **52**(10), 2438–2447 (2004).
7. Y. Sun, M. Y. Sy, Y.-X. J. Wang, A. T. Ahuja, Y.-T. Zhang, and E. Pickwell-Macpherson, "A promising diagnostic method: Terahertz pulsed imaging and spectroscopy," *World J. Radiol.* **3**(3), 55–65 (2011).
8. D. Y. S. Chau, A. R. Dennis, H. Lin, J. A. Zeitler, and A. Tunnacliffe, "Determination of Water Content in Dehydrated Mammalian Cells Using Terahertz Pulsed Imaging: A Feasibility Study," *Curr. Pharm. Biotechnol.* **17**(2), 200–207 (2015).
9. M. H. Arbab, D. P. Winebrenner, T. C. Dickey, A. Chen, M. B. Klein, and P. D. Mourad, "Terahertz spectroscopy for the assessment of burn injuries in vivo," *J. Biomed. Opt.* **18**(7), 077004 (2013).
10. S. Sy, S. Huang, Y.-X. J. Wang, J. Yu, A. T. Ahuja, Y.-T. Zhang, and E. Pickwell-MacPherson, "Terahertz spectroscopy of liver cirrhosis: investigating the origin of contrast," *Phys. Med. Biol.* **55**(24), 7587–7596 (2010).

11. Y. Miura, A. Kamataki, M. Uzuki, T. Sasaki, J. Nishizawa, and T. Sawai, "Terahertz-wave spectroscopy for precise histopathological imaging of tumor and non-tumor lesions in paraffin sections," *Tohoku J. Exp. Med.* **223**(4), 291–296 (2011).
12. C. S. Joseph, A. N. Yaroslavsky, V. A. Neel, T. M. Goyette, and R. H. Giles, "Continuous wave terahertz transmission imaging of nonmelanoma skin cancers," *Lasers Surg. Med.* **43**(6), 457–462 (2011).
13. R. M. Woodward, B. E. Cole, V. P. Wallace, R. J. Pye, D. D. Arnone, E. H. Linfield, and M. Pepper, "Terahertz pulse imaging in reflection geometry of human skin cancer and skin tissue," *Phys. Med. Biol.* **47**(21), 3853–3863 (2002).
14. P. Doradla, K. Alavi, C. Joseph, and R. Giles, "Detection of colon cancer by continuous-wave terahertz polarization imaging technique," *J. Biomed. Opt.* **18**(9), 090504 (2013).
15. S. J. Oh, S.-H. Kim, Y. B. Ji, K. Jeong, Y. Park, J. Yang, D. W. Park, S. K. Noh, S.-G. Kang, Y.-M. Huh, J.-H. Son, and J.-S. Suh, "Study of freshly excised brain tissues using terahertz imaging," *Biomed. Opt. Express* **5**(8), 2837–2842 (2014).
16. T. C. Bowman, M. El-Shenawee, and L. K. Campbell, "Terahertz Imaging of Excised Breast Tumor Tissue on Paraffin Sections," *IEEE Trans. Antenn. Propag.* **63**(5), 2088–2097 (2015).
17. P. C. Ashworth, E. Pickwell-MacPherson, E. Provenzano, S. E. Pinder, A. D. Purushotham, M. Pepper, and V. P. Wallace, "Terahertz pulsed spectroscopy of freshly excised human breast cancer," *Opt. Express* **17**(15), 12444–12454 (2009).
18. A. J. Fitzgerald, V. P. Wallace, M. Jimenez-Linan, L. Bobrow, R. J. Pye, A. D. Purushotham, and D. D. Arnone, "Terahertz Pulsed Imaging of Human Breast Tumors," *Radiology* **239**(2), 533–540 (2006).
19. P. Y. Han, G. C. Cho, and X. C. Zhang, "Time-domain transillumination of biological tissues with terahertz pulses," *Opt. Lett.* **25**(4), 242–244 (2000).
20. A. J. Fitzgerald, E. Berry, N. N. Zinov'ev, S. Homer-Vanniasinkam, R. E. Miles, J. M. Chamberlain, and M. A. Smith, "Catalogue of human tissue optical properties at terahertz frequencies," *J. Biol. Phys.* **29**(2-3), 123–128 (2003).
21. F. Wahaia, G. Valusis, L. M. Bernardo, A. Almeida, J. A. Moreira, P. C. Lopes, J. Macutkevicius, I. Kasalynas, D. Seliuta, R. Adomavicius, R. Henrique, and M. Lopes, "Detection of colon cancer by terahertz techniques," *J. Mol. Struct.* **1006**(1-3), 77–82 (2011).
22. D. M. Charron, K. Ajito, J. Y. Kim, and Y. Ueno, "Chemical mapping of pharmaceutical cocrystals using terahertz spectroscopic imaging," *Anal. Chem.* **85**(4), 1980–1984 (2013).
23. W. E. Baughman, H. Yokus, S. Balci, D. S. Wilbert, P. Kung, and S. M. Kim, "Observation of hydrofluoric acid burns on osseous tissues by means of terahertz spectroscopic imaging," *IEEE J. Biomed. Health Inform.* **17**(4), 798–805 (2013).
24. S. Fan, E. P. J. Parrott, B. S.-Y. Ung, and E. Pickwell-MacPherson, "Improved Algorithm for Material Characterization by Terahertz Reflection Imaging," in *2015 40th International Conference on Infrared, Millimeter, and Terahertz Waves (IRMMW-THz)* (2015).
25. B. Recur, L. Frederique, B. Bousquet, L. Canioni, and P. Mounaix, "Review of Terahertz Tomography Techniques," *J. Infrared Millim. Terahertz Waves* **35**(4), 382–411 (2014).
26. Y. B. Ji, S.-H. Kim, K. Jeong, Y. Choi, J.-H. Son, D. W. Park, S. K. Noh, T.-I. Jeon, Y.-M. Huh, S. Haam, S. K. Lee, S. J. Oh, and J.-S. Suh, "Terahertz spectroscopic imaging and properties of gastrointestinal tract in a rat model," *Biomed. Opt. Express* **5**(12), 4162–4170 (2014).
27. J. H. Son, "Terahertz electromagnetic interactions with biological matter and their applications," *J. Appl. Phys.* **105**(10), 102033 (2009).
28. T. C. Bowman, Y. Wu, A. Walter, J. Gauch, M. El-Shenawee, and L. K. Campbell, "Time of Flight THz Imaging of 3D Ex-Vivo Breast cancer Tumor Tissues," in *40th International Conference on Infrared, Millimeter, and Terahertz Waves* (2015).
29. T. Bowman, M. El-Shenawee, and L. K. Campbell, "Time of flight estimation for breast cancer margin thickness using pulsed terahertz transmission imaging," *Proc. SPIE* **9706**, 97061V (2016).
30. T. C. Bowman, "Experimental Terahertz Imaging and Spectroscopy for Ex-vivo Breast Cancer Tissue," University of Arkansas (2014).
31. T. Bowman, M. El-Shenawee, and L. K. Campbell, "Regional spectroscopy of paraffin-embedded breast cancer tissue using pulsed terahertz transmission imaging," *Proc. SPIE* **9706**, 97061W (2016).
32. "Breast Cancer." American Cancer Society [Online]. Available: <http://www.cancer.org/acs/groups/cid/documents/webcontent/003090-pdf.pdf> Last revised 4 May 2016.
33. R. Piesiewicz, C. Jansen, S. Wietzke, D. Mittleman, M. Koch, and T. Kürner, "Properties of building and plastic materials in the THz range," *Int. J. Infrared Millim. Waves* **28**(5), 363–371 (2007).
34. C. T. A. Johnk, *Engineering Electromagnetic Fields and Waves*, 2nd ed. (John Wiley & Sons, Inc., 1988).
35. S. J. Orfanidis, *Electromagnetic Waves and Antennas* (2013).
36. Z. D. Taylor, R. S. Singh, D. B. Bennett, P. Tewari, C. P. Kealey, N. Bajwa, M. O. Culjat, A. Stojadinovic, H. Lee, J. P. Hubschman, E. R. Brown, and W. S. Grundfest, "THz Medical Imaging: in vivo Hydration Sensing," *IEEE Trans. Terahertz Sci. Technol.* **1**(1), 201–219 (2011).

## 1. Introduction

Terahertz (THz) has been a greatly expanding field of research in recent years. While historically THz frequencies (0.1 to 4 THz) were difficult to access due to the gap between electronic and optical generation techniques, the advent of more reliable THz sources has

opened up this range for a wide variety of potential applications [1]. Such areas include security and explosive detection [2], semiconductor characterization and carrier dynamics [3], and nondestructive evaluation of electronic devices [4].

One focus where THz has shown particular promise is in biomedical and pharmaceutical research, where the work in THz applications has grown rapidly, especially in the field of biomedical imaging [5]. This is in large part due to THz frequencies showing significant distinctions between many different kinds of diseased and healthy tissue [6,7]. THz is particularly sensitive to water content in different types of tissue, which is a key contrast factor in many of its biomedical imaging applications [8]. As a result, THz imaging has shown promise in assessment of burns [9], liver cirrhosis [10], and tissue damage from myocardial infarction [11]. Most notably, THz imaging has been applied to detecting and assessing regions of cancer in healthy tissue for a wide range of cancers including cancer of the skin [12,13], liver [11], colon [14], brain [15], and breast [16–18].

Generally, for THz biomedical imaging there are two common orientations of the sample under test: reflection or transmission. Standard transmission imaging involves the sample placed between plates of low-absorption material or standing free in a sample space. The incident signal generated by the THz system travels at a normal incident to the sample surface and the transmitted signal is received on the other side. For THz reflection image, the reflected signal is measured on the same side as the incident signal. This is accomplished either by setting the incident and reflection signals at an oblique angle or by using a beamsplitter in order to separate the incident and reflected signals when both occur at normal incidence [14].

For biological applications, THz has been shown to propagate through several millimeters of animal fat tissue for effective imaging in transmission setups [19]. However, many bodily tissues possess significantly higher absorption in the THz range than fat due to the varying water content between healthy and diseased or damaged tissue [20]. Thus the use of THz transmission imaging for biological applications has been limited to date. Transmission imaging has been applied to thin (160-200  $\mu\text{m}$ ) sections of formalin-fixed heart and liver tissue [11], thicker (1.5 mm) sections of colon cancer embedded in paraffin [21], and thin (260  $\mu\text{m}$ ) frozen and thawed skin cancer tissue using continuous wave imaging at 1.4 and 1.6 THz [12]. In each case the sample preparation either relied on very thin tissue or on the dehydration of the sample through formalin fixing in order to maintain a reasonable transmitted signal. Because of this, reflection imaging is the more commonly used THz technique for in-vivo or fresh tissue studies. Investigations using a THz transmission setup have also shown the potential of applying spectroscopy across an imaging scan in order to perform regional solutions of the properties of the sample under test. This concept has been applied for assessment of crystal formations in pharmaceuticals [22] and in biomedical imaging for observing the degradation of bone tissue [23].

The use of imaging to obtain tissue properties has also been used in reflection orientations. The use of reflection imaging to calculate tissue characteristics is an established technique for THz applications, and various tomography techniques have also been developed for specific orientations of THz systems [24,25]. Reflection spectroscopy has been applied to the detection of water content in cells [8], assessment of liver cirrhosis [10], and in characterization of fresh animal gastrointestinal tissue [26]. A published study investigating THz interaction with DNAs, RNAs, proteins, biological liquids, and cellular structure or density demonstrated that THz contrast can be achieved without water presence [10,27]. The THz contrast is expected to increase by four times with the water content in fresh tissue [15].

Previous work by our group has focused on the reflection imaging of infiltrating ductal carcinoma in flat sections [16], and preliminary results in reflection imaging of three-dimensional tissue embedded in paraffin blocks was reported [28,29]. Preliminary work has investigated the THz transmission spectroscopy, but using only few point measurements taken from the same sample [30,31].

The motivation for this work is to compare reflection and transmission imaging of human breast carcinomas and to address the advantages and disadvantages of each. To the author's

knowledge, there is no previous work comparing THz imaging of biological tissue using both transmission and reflection orientation. While fresh tissue is highly absorbent to THz waves, which generally requires the use of reflection imaging [13,18], dehydrated (fixed) cancer tissue can be imaged using reflection and/or transmission mode. Fixed tissue is more easily obtained than fresh tissue for this imaging as well and can be used to optimize the THz imaging and investigate the contrast of cancer independent of the water content. An additional focus of this work is the development of inversion algorithms to solve for the refractive index and absorption coefficient of biological tissues in the THz range. In contrast to previously published studies on the THz properties of breast tissue, this work seeks to address significant practical issues that can hinder the acquisition of these properties while developing the methods for an eventual clinical application. The use of fresh bovine tissue is utilized in order to validate the calculation of fresh tissue refractive index and absorption coefficients.

The outline of the paper is as follows: Section 2 will address the methodology including the THz system and sample preparation; Section 3 will detail the propagation modeling; Section 4 will validate the modeling with property measurements of fresh bovine tissue; Section 5 will extend the imaging and characterization to excised human breast carcinomas; and Section 6 will address challenges and future work.

## 2. Methodology

### 2.1 Pulsed terahertz system

The measurements in this work make use of the TPS 3000 pulsed terahertz imaging and spectroscopy system from TeraVIEW, Ltd. The system diagram can be seen in Fig. 1(a). The incident terahertz pulse is directed by parabolic mirrors to the sample space for either transmission imaging (Fig. 1(a)) or reflection imaging (Fig. 1(b)). The system uses a Ti:Sapphire laser of ~100 mW to excite a GaAs antenna that generates the time domain terahertz pulse shown in Fig. 1(c). The system has interchangeable modules that permit a transmission or reflection imaging setup. For transmission the sample is mounted in a motorized frame in the focal center of the incident beam and the transmitted signal is measured. Both the emitter and detector are positioned at normal angle to the sample under test. For reflection the sample is mounted on a motorized stage, and a parabolic mirror base directs the incident signal to focus at the surface of reflection. The reflected signal is then collected in the system. Both the emitter and detector are positioned at 30° oblique to the sample under test. In either case the signal is obtained by measuring the generated bias from a receiving antenna excited by the THz signal and an optically coherent laser pulse split from the original source. The sample space of the system is purged with dry nitrogen gas while in use in order to reduce any absorption from water vapor in air. The THz signal generated in the system has an approximate beam width of 500 fs. The use of Fourier transform of the pulse provides an effective frequency range of 0.1 to 4 THz that can be seen in Fig. 1(d). This allows for imaging or calculation of sample properties at several frequencies from a single time domain measurement. The output THz power of the system is approximately 1  $\mu$ W.

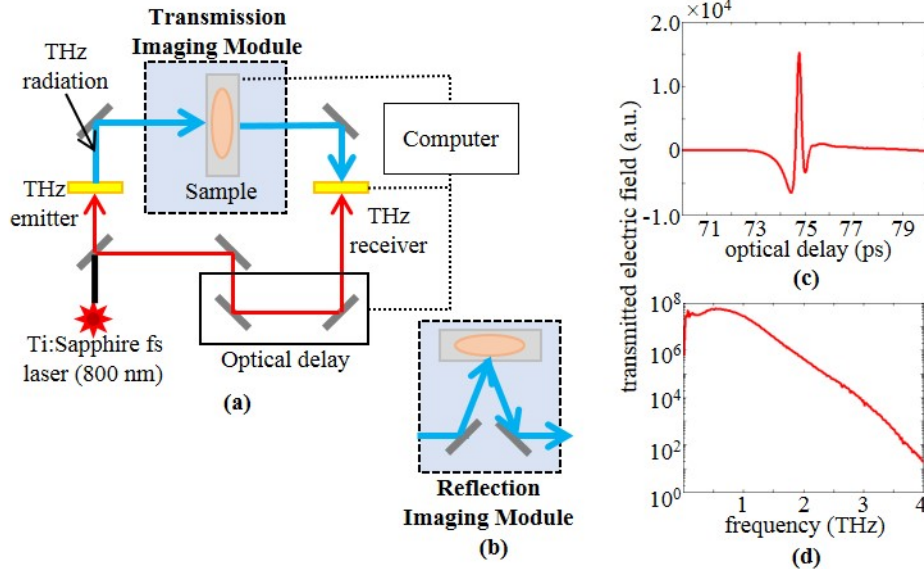


Fig. 1. TPS Spectra 3000 (a) diagram with transmission imaging module, (b) reflection imaging module, (c) incident time domain signal, and (d) frequency domain signal obtained with Fourier transform.

## 2.2 Sample preparation

The first excised breast cancer tissue sample used in this work was obtained through Northwest Arkansas Pathology Associates, P.A in collaboration with Dr. Lucas Campbell. The sample was obtained from a 69 year old patient diagnosed with stage II/III lobular carcinoma. Another sample was obtained through the National Disease Research Interchange (NDRI) from a 39 year old patient diagnosed with stage III/III infiltrating ductal carcinoma. The tissues were originally provided as formalin-fixed, paraffin-embedded (FFPE) blocks and were later sectioned into 20, 30, and 40  $\mu\text{m}$  thick tissue slices on polystyrene microscope slides. For the purpose of this work, 20 and 30  $\mu\text{m}$  sections are used. Between each tissue section, a 5  $\mu\text{m}$  thick section is sliced, mounted on a standard glass microscope slide, and subjected to staining with hematoxylin and eosin (H&E) for the purpose of pathology assessment and correlation to the THz images. No staining or any contrast agents are applied to the sections used in THz imaging. The tissues selected in this work represent the two most common breast cancer types. Infiltrating ductal carcinoma accounts for approximately 8 out of every 10 invasive breast cancer diagnoses, while lobular carcinoma accounts for 1 of 10 [32].

## 2.3 Selection of slide materials

Previous work with FFPE tissue in our group dealt primarily with tissue on glass slides [16,30]. However, this posed a significant problem with regards to the ability to perform transmission spectroscopy of the tissue due to the strong attenuation of glass in the THz range [30]. In order to have better transmission, polystyrene microscope slides of 3"  $\times$  1" with an average thickness of 1 mm are selected due to their low absorption in the THz range compared to other standard polymers [33]. For imaging and validating the solution of the properties of fresh bovine tissue, a 1.2 mm thick polystyrene (Plaskolite) plate of 3"  $\times$  3" was placed on the system to hold the fresh meat in the reflection setup, as will be detailed in Section 4. The properties of the two kinds of polystyrene are measured using a basic THz spectroscopy setup for a single material in air. The results are shown in Fig. 2. It can be clearly seen that the two types of polystyrene have very similar properties and relatively low

absorption across the entire frequency range used in this work. Thus the material is suitable for both transmission and reflection imaging of tissue.

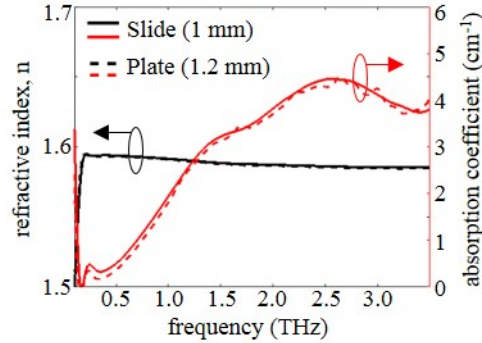


Fig. 2. The refractive index (black) left scale and absorption coefficient (red) right scale of two polystyrene materials used in this work: a 1 mm thick microscope slide (solid line) and 1.2 mm thick polystyrene plate (dotted line).

### 3. Propagation modeling

#### 3.1. Transmission mode

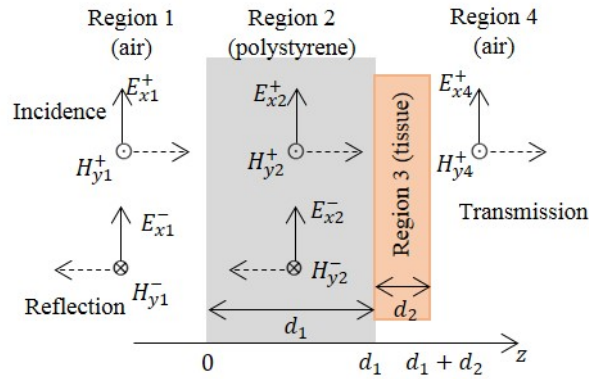


Fig. 3. Transmission imaging setup.

In order to obtain the properties of the breast carcinomas in this work, modeling is set up to compare the theoretical propagation of the THz signal to the measured signal. The transmission setup for FFPE tissue mounted on a polystyrene slide can be seen in Fig. 3. In this measurement orientation the incident terahertz signal encounters the polystyrene first then the tissue before being collected at the receiver. While the sample measurement is selected as the transmission through both polystyrene slide and FFPE tissue, the reference signal can be taken from the transmission through air or the transmission through the polystyrene slide alone. Since the properties of the polystyrene can be measured separately as shown in Fig. 2, a blank slide serves as the reference in this case. The propagation of the signal through both the sample and reference points is calculated using well-established impedance and reflection interactions for multiple layers [34,35]. The ratio of the sample to the reference signal takes the form

$$E_{\text{sample}} / E_{\text{ref}} = \tilde{\tau} e^{(\gamma_1 - \gamma_3) d_2}, \quad (1)$$

where  $\tilde{\tau}$  is the ratio between the transmission coefficients of the two measurements and  $\gamma_i = j(\omega/c)\tilde{n}_i$  is the complex propagation coefficient of region  $i = 1, 2, 3, \dots$ , with  $\omega$  indicating the angular frequency,  $c$  is the speed of light in vacuum, and  $\tilde{n}_i$  as the complex refractive index of the region. This can be further expressed as  $\tilde{n} = n - j\frac{c}{2\omega}\alpha_{abs}$ , where the real refractive index  $n$  and the power absorption coefficient  $\alpha_{abs}$  are the properties being calculated in this work. The term  $\tilde{\tau}$  is given by

$$\tilde{\tau} = \left( \frac{2\tilde{n}_3(\tilde{n}_1 + \tilde{n}_2)}{(\tilde{n}_1 + \tilde{n}_3)(\tilde{n}_2 + \tilde{n}_3)} \right) \left( \frac{1 - \rho_{12}^2 e^{-2\gamma_2 d_1}}{1 + \rho_{23}\rho_{31} e^{-2\gamma_3 d_2}} \right) \left( 1 + \rho_{12} \frac{\rho_{23} + \rho_{31} e^{-2\gamma_3 d_2}}{1 + \rho_{23}\rho_{31} e^{-2\gamma_3 d_2}} e^{-2\gamma_2 d_1} \right)^{-1}. \quad (2)$$

Here  $\rho_{ij}$  is the Fresnel reflection coefficient for normal incidence between regions  $i$  and  $j$  in the setup of Fig. 3, given by  $\rho_{ij} = (\tilde{n}_i - \tilde{n}_j) / (\tilde{n}_i + \tilde{n}_j)$ . The first term in the numerator is the ratio between the Fresnel transmission coefficients in the sample and the reference, while the remaining terms are all multiple reflection contributions of the Fabry-Perot effect in each region. For the case of carcinoma on a polystyrene slide, the thickness of the polystyrene is  $d_1 = 1$  mm and the tissue thickness is  $d_2 = 20$ -30  $\mu\text{m}$ . Although the absorption of the polystyrene is low and multiple reflections do exist in this layer, all second reflections are windowed out during measurements by adjusting the time scale in the system. In order to have consistency in the model with the measurements in this case, all  $\exp[-2\gamma_2 d_1]$  terms in Eq. (2) are assumed zero. In order to obtain the properties of the tissue (region 3), Eq. (1) is numerically solved for a range of  $n_3$  and  $\alpha_{abs,3}$  and the error between both the magnitude and phase of the measured  $E_{samp} / E_{ref}$  and the calculated transmission is given by

$$err_{mag} = \left[ \ln \left( \left| E_{samp} / E_{ref} \right| \right)_{meas} \right] - \left[ \Re \{ \ln(\tilde{\tau}) \} + (\alpha_{abs,1} - \alpha_{abs,3}) \frac{d_2}{2} \right], \quad (3)$$

and

$$err_{phase} = \left[ \arg \left( E_{samp} / E_{ref} \right)_{meas} \right] - \left[ \Im \{ \ln(\tilde{\tau}) \} + \frac{\omega}{c} (n_1 - n_3) d_2 \right]. \quad (4)$$

The values of  $n_3$  and  $\alpha_{abs,3}$  for which the summed magnitudes of Eqs. (3) and (4) are simultaneously minimized are then considered to be the solutions. An inversion algorithm solves for the error between the measurement data and calculated transmission from a matrix of potential solutions using different values of the refractive index and absorption coefficient. The properties are then retrieved from the solution in the matrix with the lowest total error. To obtain a transmission image of the tissue properties, this technique is applied across every pixel in the scan for each desired frequency.

In order to reduce noise in the spectroscopy based image, two special considerations are accounted for in the measurements. In particular, the signal at the ends of the time domain measurement window is not necessarily zero, and the difference in values at this boundary can contribute high frequency noise to the measurements. To reduce this effect, a four-term Blackman-Harris filter is used to isolate the primary transmission peak in the reference and each measurement signal. Secondly, the optical delay between the reference and sample measurements is adjusted to have the peaks aligned to avoid any spectrum shifts based on the position of the peak in the time domain window. This optical delay shift is then applied to the time domain signal of the measurements when obtaining the measured magnitude and phase.

### 3.2 Reflection mode

The setup for the reflection mode can be oriented in several ways based on the positioning of the sample. The polarization of the beam with respect to the sample will affect the resulting

reflection. This work investigates three different reflection setups, which are shown for the *TM* (parallel) mode in Fig. 4 [35]. In Fig. 4(a), the incident THz signal encounters the tissue first then the polystyrene slide. Additional orientations shown in Fig. 4(b) and Fig. 4(c) are also investigated in this work. For the sake of space only the formulation for the setup in Fig. 4(a) will be given here, while the expressions for the cases in Fig. 4(a) and 4(b) are slightly different. In all measurements here, secondary reflections are windowed out as explained in Sec. 3.1.

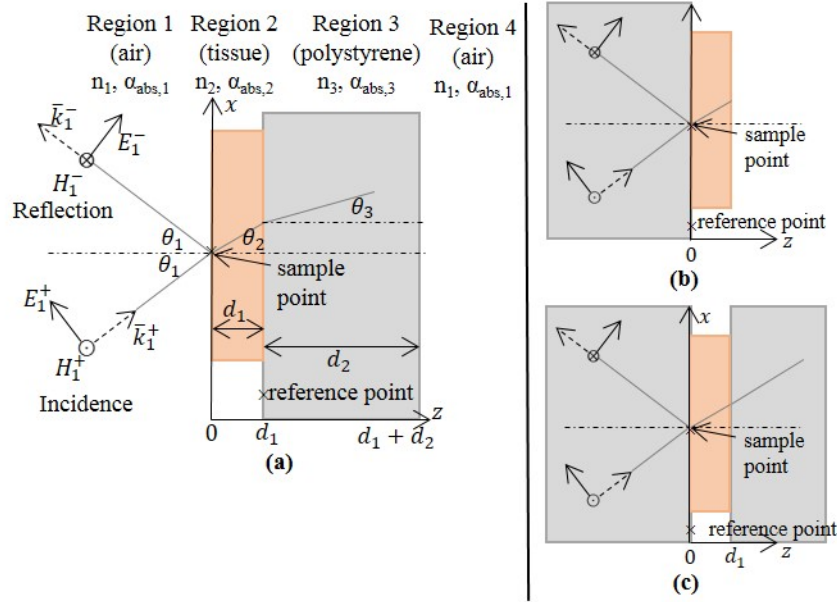


Fig. 4. Reflection imaging setups for tissue on polystyrene slides. (a) Air, tissue, polystyrene slide, air orientation. (b) air, slide, tissue, air orientation. (c) air, slide, tissue, slide, air setup. In all cases, the THz emitter and detector are located on the left side.

For the setup in Fig. 4(a), the sample reflection is collected from the surface of the tissue, while the reference signal is collected from the same polystyrene slide with no tissue. The resulting ratio of the sample and reference signals is given by

$$\frac{E_{samp}}{E_{ref}} = \Gamma_T = \left( \frac{\rho_{T,12} + \rho_{T,23} e^{-j2\frac{\omega}{c}\tilde{n}_2 \cos\theta_2 d_1}}{1 + \rho_{T,12}\rho_{T,23} e^{-j2\frac{\omega}{c}\tilde{n}_2 \cos\theta_2 d_1}} \right) \frac{1}{\rho_{T,13} e^{-j2\frac{\omega}{c}\tilde{n}_1 \cos\theta_1 d_1}}, \quad (5)$$

where  $\rho_{T,ij}$  is the Fresnel reflection coefficient between regions  $i$  and  $j$  for the oblique incidence in the reflection mode where its expression depends on the polarization of the beam (see Appendix A). The difference in distance between the sample points on the tissue surface and the reference point on the polystyrene slide in Fig. 4(a) is accounted for through the phase term ( $\exp(-j2\frac{\omega}{c}\tilde{n}_2 \cos\theta_2 d_1)$ ) in the denominator of Eq. (5). The angle of incidence in air is known ( $\theta_1 = 30^\circ$ ), so the angles of propagation in each region are defined using Snell's Law

$$\tilde{n}_1 \sin\theta_1 = \tilde{n}_2 \sin\theta_2 = \tilde{n}_3 \sin\theta_3. \quad (6)$$

In order to obtain a reflection image of tissue properties (i.e. the refractive index and absorption coefficient at each pixel), the polarization of the THz beam needs to be known (i.e. *TE* or *TM*). However, due to the parabolic mirrors used to orient the reflection beam in the measurement system, the polarization of the beam is believed to be a hybridization of *TE* and *TM* modes that could not be determined analytically. Instead, for this work the polarization of

the detected signal is approximated experimentally by first measuring the electrical properties of an acrylic sheet using fixed point spectroscopy. Then the reflection from the acrylic is calculated for the  $TE$  and  $TM$  polarizations with accounting for potential rotations between the two polarizations from  $0^\circ$  to  $90^\circ$  as shown in Fig. 5. The calculated reflections at these rotation angles  $\psi$  and the measurement signal are compared versus frequency in Fig. 5.

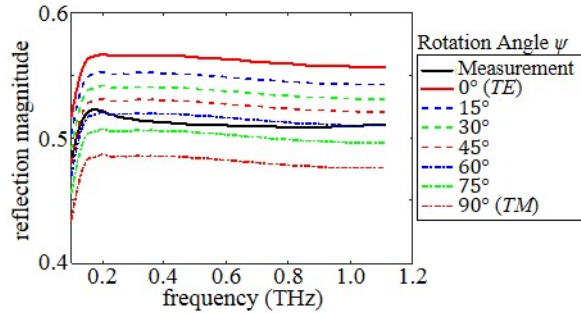


Fig. 5. Calculated reflection signals at different rotation angle  $\psi$  between  $TE$  and  $TM$  modes versus the measurement signal for acrylic sheet.

From the comparison in Fig. 5, it becomes clear that while neither  $TE$  nor  $TM$  mode accurately models the reflection signal in the measurement system, a combined reflection with polarization rotation angle of  $\psi = 60^\circ$  with respect to  $TE$  mode gives a good estimation of the received signal. The resulting calculated reflection ratio is expressed as

$$E_{samp}/E_{ref} = \Gamma = \sqrt{(\Gamma_{TE} \cos \psi)^2 + (\Gamma_{TM} \sin \psi)^2}, \quad (7)$$

where  $\Gamma_{TE}$  and  $\Gamma_{TM}$  are the individual solutions to Eq. (5) for  $TE$  and  $TM$  polarizations (see Appendix A). Equation (7) is used in all reflection images presented in this work. Finally the unknown properties of the tissue in region 2 in Fig. 4a are obtained by calculating the error for a range of  $n_2$  and  $\alpha_{abs,2}$  using

$$err_{mag} = \left[ \ln \left( \left| E_{samp} / E_{ref} \right|_{meas} \right) \right] - \left[ \Re \{ \ln(\Gamma) \} \right], \quad (8)$$

and

$$err_{phase} = \left[ \arg \left( E_{samp} / E_{ref} \right)_{meas} \right] - \left[ \Im \{ \ln(\Gamma) \} \right]. \quad (9)$$

Unlike the transmission case in Eqs. (3) and (4), there are no explicit  $n_2$  and  $\alpha_{abs,2}$  in Eqs. (8) and (9) due to the absence of significant propagation in the polystyrene slide in the reflection mode compared to the transmission mode, but these unknowns are included in  $\Gamma$ . The solutions of the refractive index and absorption coefficient are obtained upon simultaneously minimizing the error expressions in Eqs. (8) and (9). For the other setups in Fig. 4b and Fig. 4c, similar equations to Eq. (5) are obtained accounting for different sequences of layers, and the additional phase term ( $\exp(-j2 \frac{\omega}{c} \tilde{n}_1 \cos \theta_1 d_1)$ ) in the denominator is absent since the tissue and reference points are at the same interface (expressions are not shown). The error Eqs. (8) and (9) are the same in all setup cases of Fig. 4.

#### 4. Validation of models

Fresh portions of bovine chuck steak are selected to validate the models of Section 3. However, because of the high absorption of THz signal in these tissues, only the reflection model can be validated. The transmission model was validated in previous work in comparison with published data of glass and polystyrene [30,31].

#### 4.1 Animal tissue spectroscopy

The diagram of the sample and reference setups and the results of the average properties are given in Fig. 6. Here the reference measurement through the quartz window and the sample transmission setup can be seen in Fig. 6(a) and Fig. 6(b). The reference signal is collected as the transmission through the two quartz windows with no plate in between shown in Fig. 6(a). The sample signal is collected from the fresh bovine tissue sliced very thin and placed in a liquid sample holder consisting of two 3 mm thick quartz plates (Fig. 6(b)). Pressure is applied to the outside of the plates in order to compress the tissue sample, and Teflon spacers around the outside edge are used to maintain a specific thickness of the tissue between the two plates. For the fat tissue a thickness of 500  $\mu\text{m}$  is sufficiently thin to get a transmitted THz signal across the entire frequency range of the measurement system. However, for the more absorptive muscle tissue the thickness needed to be reduced to 100  $\mu\text{m}$ . All single point spectroscopy measurements are averaged over 7200 time domain collected signals. Seven different samples are used for each tissue type. The properties of water are also measured here using the sample liquid holder in Fig. 6(b) with a separation of 100  $\mu\text{m}$ . All spectroscopy measurements of bovine tissue and water were conducted at room temperature (295 K).

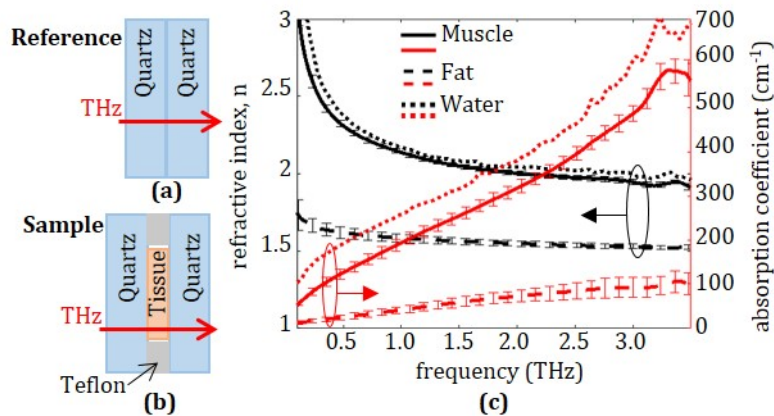


Fig. 6. THz spectroscopy of fresh bovine tissue using (a) quartz window reference and (b) sample measurement of tissue in quartz holder (c) the mean calculated refractive index (black) and absorption coefficient (red) of the muscle (solid line) and fat (dashed line). Error bars indicate the standard deviation of the measurements. The measured properties of water (dotted line) are also shown for comparison.

The results of the bovine tissue spectroscopy in Fig. 6(c) show a good differentiation between muscle and fat tissue for both refractive index and absorption coefficient. This is a well-known contrast between these tissue types in THz band as reported in the literature for human tissue [36]. These results will be used for validation of the reflection imaging models in Section 4.2. The standard deviations of the calculated values of refractive index and absorption coefficient for the muscle and fat are represented by the error bars on each plot. The same properties of water are also shown in Fig. 6 for comparison with the fresh bovine tissue. The results in Fig. 6 show the significant absorption of water that will be present in fresh tissue and will play a role in THz image contrast, in agreement with [8,10,15].

#### 4.2 Reflection imaging and calculation of tissue properties

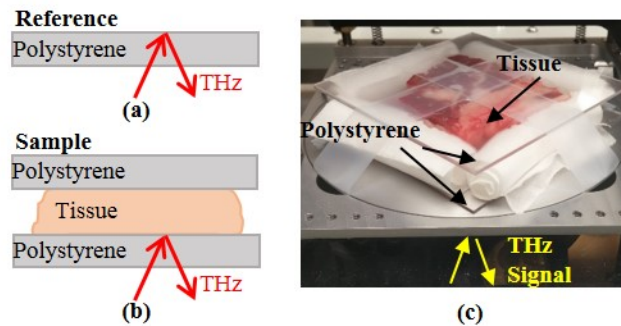


Fig. 7. Reflection imaging setup where bovine tissue is held between two polystyrene plates. (a) The reference measurement, (b) the sample measurement, and (c) photo of the sample positioned on the system window. The THz emitter and detector are positioned below the window.

Fresh bovine tissue of size  $\sim 3.5 \text{ cm} \times 3.5 \text{ cm} \times 2.5 \text{ cm}$  is scanned to obtain peak time domain, magnitude, and phase THz images. Also the measured data are used to calculate the refractive indices and absorption coefficients at each pixel in the scan to produce tissue property images. The imaging setup can be seen in Fig. 7. In this setup a polystyrene plate is used to place the fresh tissue on the imaging stage (window) and a second plate is placed on top of the tissue to apply pressure and enforce a flat surface at the focus of the THz beam. The setup is compressed manually until the tissue is flat and then held in place with tape. As a result, the tissue thickness is reduced to  $\sim 1 \text{ cm}$  during the imaging process. Clean room wipes are placed between the plates surrounding the tissue, but outside of the scanning area, to prevent leaking of blood onto the system. The reference signal is collected from the reflection of an empty polystyrene plate (no tissue) as shown in Fig. 7(a). All sample measurements were aligned to the reference based on the reflection from the bottom of the polystyrene plate as shown in Fig. 7(b). The model for the reflection setup in Fig. 4(b) is also investigated and the difference in solutions is found to be negligible due to the substantial thickness and high absorption of the bovine tissue.

The first bovine sample is shown in Fig. 8. The photograph of the tissue in Fig. 8(a) shows the two primary tissue types in this sample, with the white region primarily denoting fat and pink and red regions denoting muscle and blood. The image representing the peak of the time domain reflected signal at each pixel is shown in Fig. 8(b), where the muscle and the fat can be clearly distinguished and compared against the photograph. Here the muscle shows a significant reflection compared to the fat tissue. This is an expected result due to the much higher contrast of the properties between the muscle and the polystyrene plate compared with those between the fat and polystyrene. It should be noted that all THz images presented in Figs. 8(b)-8(j) are obtained upon manually applying pressure to flatten the tissue while the photo in Fig. 8(a) was obtained before applying that pressure. As a result, the shape of the fat region appears more spread apart in the THz images compared with the original photo. This shape spreading could be accounted for by measuring the compression force and the elasticity of the tissue, but it is outside the scope of this work.

The Fourier transform is conducted on the time domain pulse at each pixel in the scan to obtain the magnitude and phase of the reflected signal taken against a blank polystyrene reference, as seen in Fig. 8. The magnitude images, normalized against the reference, can be seen at 1 THz in Fig. 8(c) and at 2 THz in Fig. 8(d). Both frequency domain images show good distinction between the muscle and fat tissues. The reflected magnitude at 2 THz show lower values than that at 1 THz due to increased losses including higher absorption in the polystyrene plate at that frequency as well as lower refractive index in both tissues as the frequency increases in consistence with Fig. 6(c).

The reflected phase images are shown at 1 THz in Fig. 8(e) and at 2 THz in Fig. 8(f). While the general shape of the fat and muscle tissues can be seen in the phase image, the details of the tissue are not as clearly resolved as in the magnitude images. This is primarily due to the phase in the tissue region being entirely dependent on the phase shift from the reflection at the polystyrene/tissue interface rather than from any propagation in the tissue (tissue is highly absorbing). However, this also made the phase measurement highly sensitive to any curvature of the polystyrene plate, as small offsets in the position of the reflection peak are attributed to phase variations in the reflection. When necessary, small variation in the polystyrene position is corrected by shifting the measurement signal to align to the first reflection from the bottom of the polystyrene.

The magnitude and phase data are used to obtain the absorption coefficient and index of refraction of the tissue using the reflection model. The calculated refractive index images at 1 THz is shown in Fig. 8(g) and at 2 THz is shown in Fig. 8(h). The absorption coefficient is shown at 1 THz in Fig. 8(i) and at 2 THz in Fig. 8(j). The calculated properties show good agreement with the spectroscopy results in Fig. 6(c), with the refractive index of the muscle being close to the average value of 2.14 at 1 THz and decreasing to 2.0 at 2 THz. The refractive index of the fat shows a less significant reduction from 1.58 at 1 THz to 1.55 at 2 THz in the spectroscopy, which cannot be as clearly seen in the refractive index images. Likewise, the absorption coefficient can be seen increasing significantly as the frequency increases, and the results in the images are in good agreement with the measured transmission spectroscopy in Fig. 6(c).

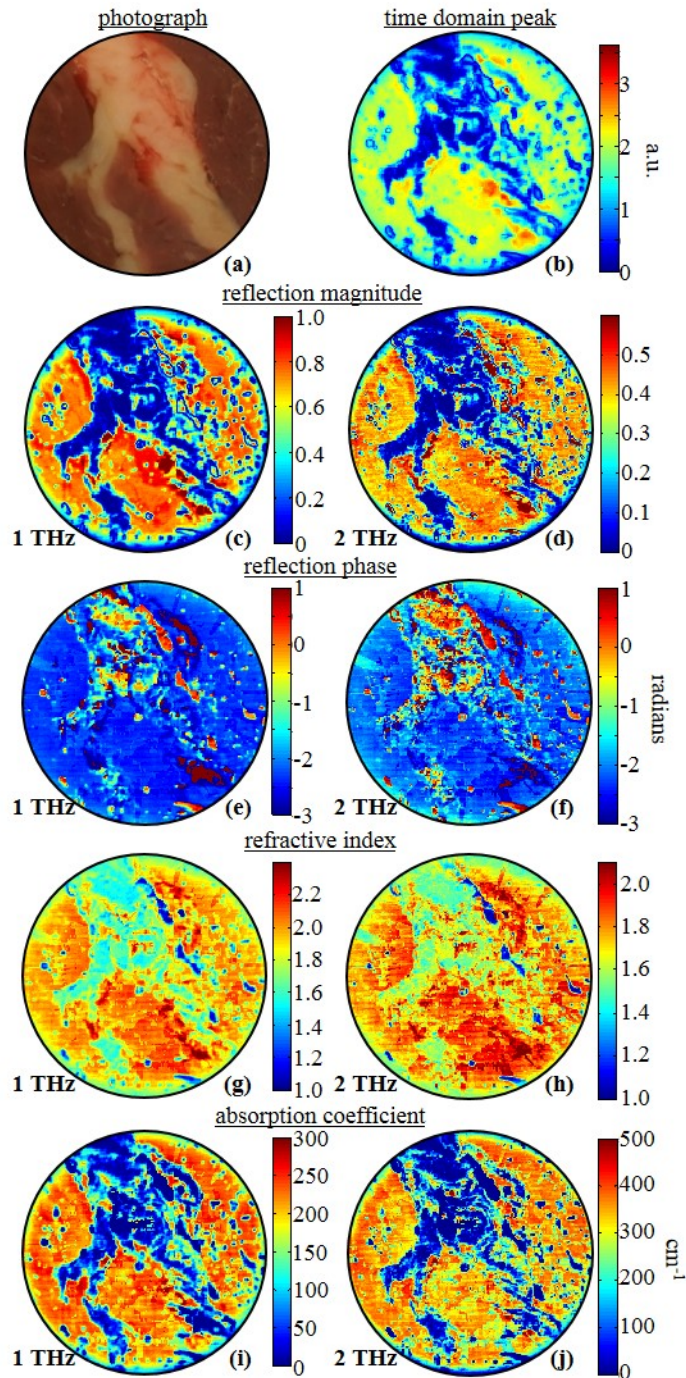


Fig. 8. Reflection imaging and characterization of fresh bovine tissue. (a) Photograph of the sample. (b) THz time domain measured reflection from sample. Fourier transform used to obtain THz frequency domain reflected magnitude at (c) 1 THz and (d) 2 THz and reflected phase at (e) 1 THz and (f) 2 THz. The calculated refractive index at (g) 1 THz and (h) 2 THz and the calculated absorption coefficient at (i) 1 THz and (j) 2 THz.

Few spots are observed in the solution images that do not look similar to the muscle or fat. Most notably, regions where the solved refractive index is 1 and absorption coefficient is 0, such as those on the top right edge of the fat tissue, indicate air gaps between the polystyrene and tissue that the applied pressure did not fully remove. Also, the large spots of higher refractive index seen around the bottom right area of the fat indicate that the blood from the tissue has pooled as evident by the slight difference with the muscle tissue.

The solution of the reflection imaging is further tested on a second sample of bovine tissue and compared across several frequencies in order to investigate the reconstruction algorithm. The results can be seen in Fig. 9 for the tissue photograph shown in Fig. 9(a). The peak time domain reflection image can be seen in Fig. 9(b). It should be noted that in this tissue sample there is a blood vessel in the center of the fat region that can be clearly seen in Fig. 9(a) and that subsequently appears in the THz image. Also, just below that blood vessel there is a region of connective tissue that appears white in the photograph but has no adipose tissue. As a result, the blood vessel and connective tissues areas appear, in all images in Fig. 9, indistinguishable from the highly hydrated muscle tissue surrounding the fat. Overall the THz images sufficiently distinguish between muscle and fat regions. Rather than looking at magnitude and phase, the solution values of refractive index and absorption coefficient images are shown for several frequencies. While the 0.5 THz images in Fig. 9(c) and Fig. 9(d) do not possess as much spatial resolution, they provide significant contrast between the muscle and fat regions. The same observation can be seen for the solution images at 0.75 THz in Fig. 9(e) and Fig. 9(f). As the frequency increases, the solution images become more subject to noise in the measurements. This most noticeably begins to arise in the images at 1 THz, where the refractive index shown in Fig. 9(g) remains distinct between the fat and muscle, but the absorption coefficient in Fig. 9(h) starts to exhibit noise in the muscle region.

Of particular note is the slight blurring of the solution around the edges of the image shown in the top edge in Fig. 9(h). This is primarily due to the slight shifting of the phase due to curvature of the polystyrene plate that could not be completely accounted for numerically. This time domain shift has a greater bearing on the phase and the subsequent solution as the frequency increases. The solution at 2 THz for both refractive index in Fig. 9(i) and absorption coefficient in Fig. 9(j) is subject to a greater amount of noise, particularly in the absorption coefficient image. This can be avoided in the future by performing signal averaging of the measurement at each point (no signal averaging is conducted here). Also, more selective windowing can be implemented to remove all measurement artifacts from early or late reflections, which can contribute high frequency noise to the solution. Nevertheless, in general the obtained properties show strong agreement with the spectroscopy in Fig. 6(c).

In both of the bovine tissue samples presented here, the fat and muscle tissue showed clear contrast in both THz time and frequency domain images and in the reconstructed electrical properties. Thus the characterization using THz reflection mode has been shown to be effective for calculating the tissue properties. This methodology can also be applied to freshly excised breast cancer tissue in the future. Challenges seen from the animal tissue here include achieving full contact of the fresh tissue to the polystyrene plate. These gaps beneath the tissue can be filled with either blood or air, resulting in scattered spots of much higher or lower reflection in the imaging as seen in Figs. 8 and 9. While these effects can be improved by using some tool to apply uniform pressure to the back of the tissue, this comes as a tradeoff with distorting the tissue dimensions leading to larger THz images compared with the physical tissue. Additionally, while the high absorption of fresh tissue limits the capability for transmission imaging, the presence of water in the tissue can greatly improve the contrast in the resulting THz reflection images [10,15].

In order to optimize the process for imaging of fresh breast cancer tissue, the primary adjustment to the methodology in this work is the development of a more standardized sample holder for mounting the tissue samples for THz imaging. While the fresh tissue imaging here used polystyrene plates and pressure was applied using tape, a clamp-based mount can be used to offer consistent pressure on the tissue. Additionally, a permanent sample holder can

be outfitted with a suitable imaging window that can provide a uniformly flat surface so that the tissue properties can be more accurately obtained. Finally, this will allow for standardized reference measurements that can be used for effective differentiation of breast cancer from normal tissue in a clinical setting.

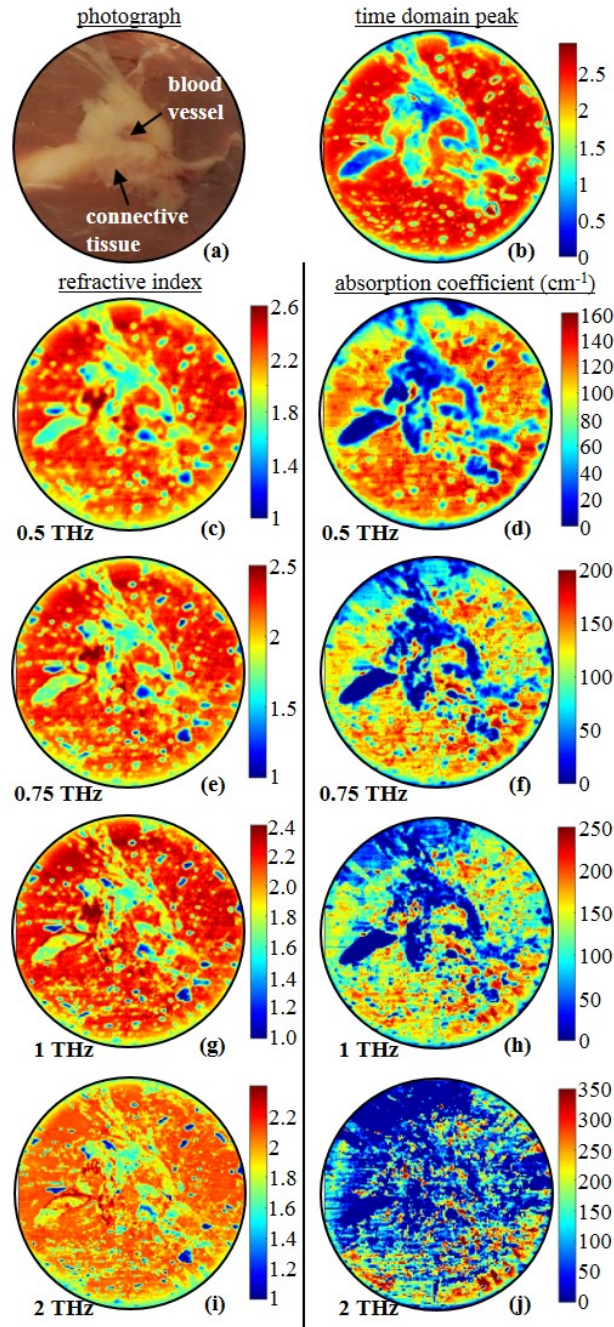


Fig. 9. Reflection imaging and characterization of bovine tissue sample 2 represented by (a) photograph. (b) The time domain reflection image, (c) the refractive index,  $n$ , and (d) the absorption coefficient,  $\alpha_{\text{abs}}$ , at 0.5 THz, (e)  $n$  and (f)  $\alpha_{\text{abs}}$  at 0.75 THz, (g)  $n$  and (h)  $\alpha_{\text{abs}}$  at 1 THz, and (i)  $n$  and (j)  $\alpha_{\text{abs}}$  at 2 THz.

## 5. Imaging of breast carcinoma

In Sec. 5.1, the processes introduced in Secs. 3 and 4 will be employed on FFPE breast lobular carcinoma. Sec. 5.1.1 will detail THz transmission and reflection imaging, and Sec. 5.1.2 will show the refractive index and absorption coefficient solution images. The same details will be shown for FFPE infiltrating ductal carcinoma in Sec. 5.2.

### 5.1 Case 1: lobular carcinoma (LC)

#### 5.1.1 Transmission and reflection images of LC

All setups shown in Sec. 2 for imaging and calculation of tissue properties are implemented and compared for the lobular carcinoma samples. First, transmission and reflection imaging are investigated for two 30  $\mu\text{m}$  thick samples taken from the same tumor block. For each sample a 5  $\mu\text{m}$  section is also sliced and treated with standard pathology dyes hematoxylin and eosin (H&E). The low power pathology regions are defined for Sample 1 in Fig. 10(a) and Sample 2 in Fig. 10(b). These two sample sections were sliced from the block at  $\sim 200 \mu\text{m}$  from each other. The lobular carcinoma of the sample is indicated by the dark purple H&E stain on the right, while the lighter pink region to the left indicates the fibroglandular tissue and the mostly clear areas indicate a mixture of fatty/fibroglandular tissue. Six positions designated 1-6 are selected in Sample 2 for more thorough pathology assessment that will be discussed in Fig. 12.

The THz reflection images of the FFPE lobular tissue are shown in Fig. 10(c) for Sample 1 and Fig. 10(d) for Sample 2. The imaging used the setup with the signal encountering the tissue first as shown in Fig. 4(a). It should be noted that the area outside of the tissue section in the THz images is paraffin. The same outlines from the pathology are applied to the THz images. The results in Figs. 10(c) and 10(d) show that the lobular carcinoma regions exhibit significantly higher reflection than the other regions. It is observed also that the mixture of fatty/fibroglandular tissue region exhibit reflection values between the carcinoma and fibroglandular. The fibroglandular tissue region exhibits the lowest reflection values. All reflection values represent electric fields in arbitrary units. In Fig. 10(d), it is noted that the THz imaged tissue extends beyond the outlines established in the pathology images. This is primarily due to the slight difference in the tumor block structure where the pathology sections and THz sections were sliced. Depending on the technique used for slicing the tissue, as much as 100  $\mu\text{m}$  of tissue could exist between the pathology and THz sections such that the tissue at lower extents in the block could be slightly larger. Regardless, the results of Figs. 10(c) and 10(d) show contrast between the carcinoma, fibroglandular and fatty/fibroglandular regions. However, there are some spots seen in the THz images that are not indicated in the pathology. For example, around the right edge of the carcinoma region, there is a dark blue area that is due to a raised edge of the tissue where it has separated from the slide. This occurs consistently in both samples in Figs. 10(c) and 10(d).

The time domain transmission images are shown in Fig. 10(e) for Sample 1 and Fig. 10(f) for Sample 2. For the THz measurement system used in this work, the transmission stage is limited in its movement range such that this entire tissue could not be imaged. Thus while it is presented to scale with the reflection images, there is a portion of the fibroglandular and fatty tissue regions that cannot be visualized. The difference in the size of Fig. 10(e) and Fig. 10(f) is due to a  $\sim 1 \text{ mm}$  difference in positioning the tissue in the two scans. In the transmission mode the different regions of the tissue are clearly defined, with the lobular carcinoma showing the least transmission, followed by the fibroglandular and then the fatty/fibroglandular tissue. The area where the tissue has separated from the slide can be clearly seen as the region of dark blue on the right side of the carcinoma region. Of note is that the transmission image does not distinguish much between the fatty/fibroglandular regions and the surrounding paraffin as shown in Figs. 10(e) and 10(f). On the other hand, these two regions are clearly distinguished in the reflection images in Figs. 10(c) and 10(d). In order to understand this issue, more thick tissue sections need to be investigated. In both samples the reflection mode demonstrate more clear contrast and higher resolution in the

margins between regions compared with the transmission mode. All images are obtained using scanning step size of  $200\ \mu\text{m}$ . The transmission imaging used an average of 4 signals at each pixel while the reflection imaging used a single signal at each pixel.

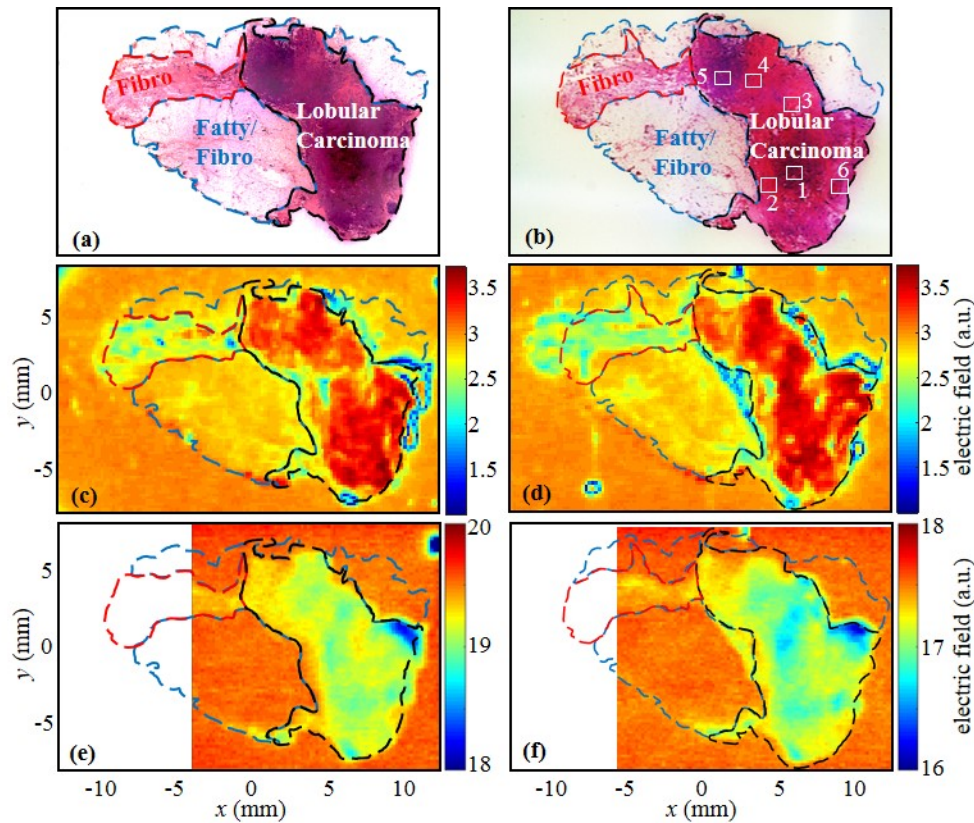


Fig. 10. Reflection and Transmission images of lobular carcinoma samples obtained from 69-year-old woman. Pathology of (a) Sample 1 and (b) Sample 2 with regions designated by outlines for lobular carcinoma (black), fibroglandular (red), and fatty/fibroglandular (blue) tissue. Points 1-6 are indicated for high power pathology assessment to be shown in Fig. 12. Reflection peak time domain images are shown for (c) Sample 1 and (d) Sample 2. Transmission peak time domain images are shown for (e) Sample 1 and (d) Sample 2. Blank areas in the transmission images (e-f) represent the smaller scanning ranges (window size) in the transmission module in the measurement system used in this work, which is not the case for the reflection module in the system.

In Fig. 11, the Fourier transform is used to obtain images at specific frequencies that can show additional details as reported in breast infiltrating ductal carcinoma [16]. In this case the areas of both transmission and reflection modes are truncated to the same size across all images for the purpose of comparison. The pathology is also shown at this scale for Sample 1 in Fig. 11(a) and for Sample 2 in Fig. 11(b). For each imaging mode the frequency domain magnitude is shown at 1 and 2 THz. For transmission mode, the images at 1 THz are given in Fig. 11(c) and 11(d) for Sample 1 and 2 and the images at 2 THz are given in Fig. 11(e) and 11(f). It can be seen that while increasing the frequency does provide a little more distinction of the margins of the tissue regions, this comes at the expense of increasing the noise at 2 THz. Also, neither of the frequency domain images in THz show any substantial details that were not shown in the time domain transmission images in Fig. 10(e) and Fig. 10(f). Also, here the fatty/fibroglandular mixed tissue region still shows no differentiation from the paraffin region.

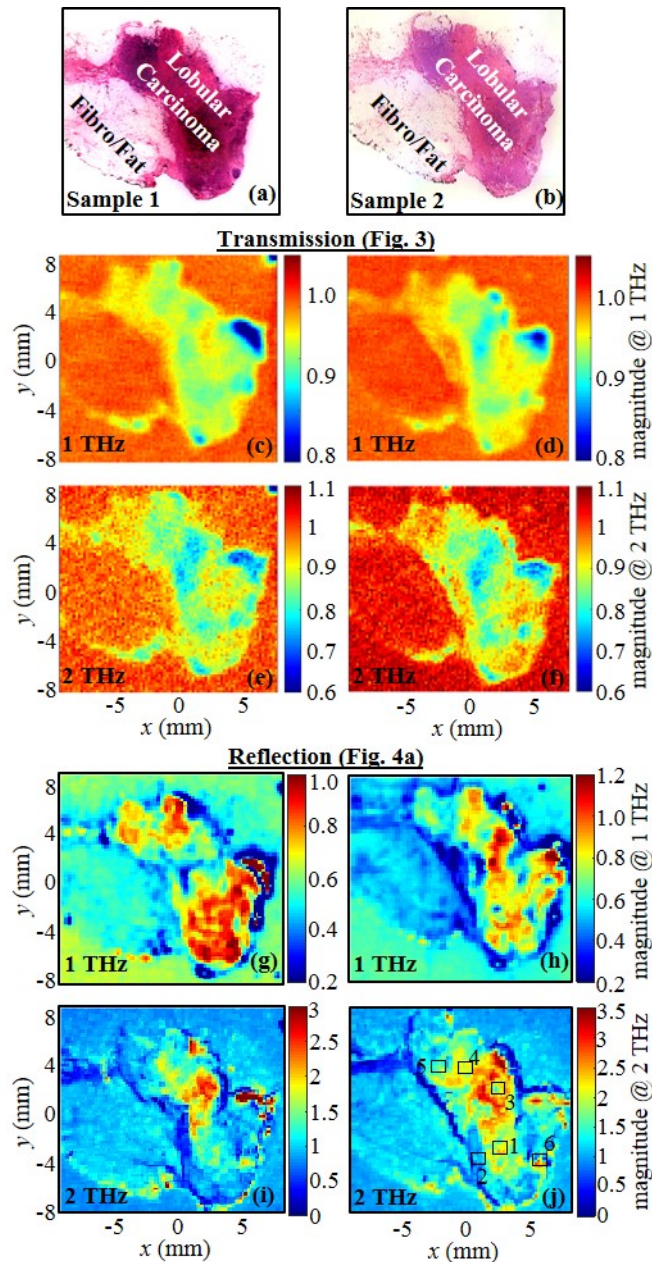


Fig. 11. Frequency domain images of lobular carcinoma. Pathology given for (a) Sample 1 and (b) Sample 2. Transmission magnitude images at 1 THz for (c) Sample 1 and (d) Sample 2 and at 2 THz for (e) Sample 1 and (f) Sample 2 following the configuration in Fig. 3. Reflection magnitude images at 1 THz for (g) Sample 1 and (h) Sample 2 and at 2 THz for (i) Sample 1 and (j) Sample 2 following the configuration in Fig. 4(a). Points labeled 1-6 in reflection images indicate features that are visible in the images compared with high power pathology in Fig. 12.

The reflection frequency domain images are shown at 1 THz for Sample 1 in Fig. 11(g) and Sample 2 in Fig. 11(h). The images at 2 THz are shown for Sample 1 in Fig. 11(i) and for Sample 2 in Fig. 11(j). While the time domain images in Fig. 10(c) and 10(d) exhibit the carcinoma as almost a homogeneous region, the reflection frequency domain images in Figs.

11(g)-11(j) exhibit a heterogeneous carcinoma region. In Fig. 11(g), the 1 THz images show clear margins between all regions, although the reflection magnitude of the electric field from the fatty/fibroglanular mixed region and mostly fibroglanular region seem similar, while the lobular carcinoma at this frequency shows higher reflection. However, of greater note is that the reflection within the lobular carcinoma itself shows heterogeneity exhibited at different positions in the region.

For Sample 1, the center of the lobular carcinoma shows much lower reflection at 1 THz than the upper and lower areas in Fig. 11(g), while the center shows a higher reflection in Sample 2 in Fig. 11(h). In the 2 THz images, the fibroglanular and fatty/fibroglanular mixed tissue regions are distinct, with the primarily fibroglanular region showing a lower reflection. The lobular carcinoma region once again shows the highest reflection, with the center area showing a consistently higher reflection than the rest of the carcinoma in Figs. 11(i) and 11(j).

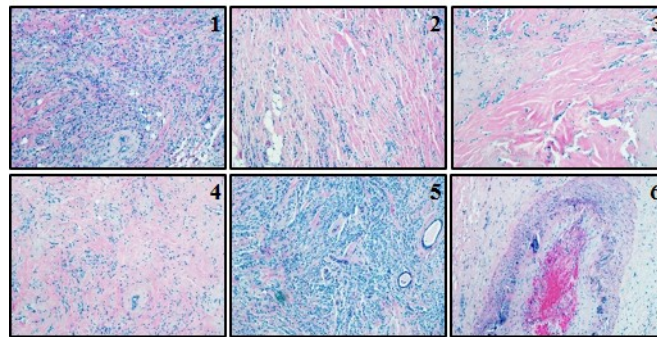


Fig. 12. High power pathology (100X) of positions 1-6 indicated in Fig. 10(b), showing neoplastic epithelial cells of varying density in positions 1-5 and a blood vessel in position 6.

In order to understand the areas of heterogeneity observed in the lobular carcinoma in the frequency domain reflection images, positions 1-6 are arbitrarily selected to obtain higher power pathology images (100X) in Sample 2. The higher power pathology images in Fig. 12 demonstrate that the tumor cells (i.e. the neoplastic epithelial component) are accompanied by varying amounts of mature collagen (the pink fibers). The tumor cells are small and blue-staining. In some areas, they are densely cellular, while in other areas they are overshadowed by the collagenous stroma. Positions 1-5 of the tumor contain neoplastic cells of varying cellular densities. In particular, positions 1 and 5 are more densely cellular as opposed to positions 2-4, which have more scant cellularity with more stroma (dense pink material). Position 6 is a large blood vessel (artery) that appears to have patchy mineralization of the vascular wall and a poorly-organized thrombus (clot) in the lumen. The differences between these positions can be most clearly seen in the 2 THz reflection images in Figs. 11(i) and 11(j), where positions 3 and 4 corresponding to the highly collagenous carcinoma show a much higher reflection than the densely cellular regions at positions 1 and 5. In both cases position 2 shows slightly lower reflection, which may indicate further difference, such as tissue adhesion to the slide, between the different areas of lower cellularity. The blood vessel at position 6 shows up as an isolated high reflection in both samples. These features were not observed in any significant sense in the transmission images in Fig. 11, indicating to another advantage of the reflection imaging of the sections used in this work.

For additional analysis of these heterogeneous areas inside the carcinoma region, the time domain reflection signals are collected at few points marked as A, B, and C shown in Fig. 13. The subsequent time domain comparison is given by Fig. 13(a) for Sample 1 and Fig. 13(b) for Sample 2. For Sample 1 the signal at point B is found to have an earlier peak position than the other two signals at A and C. Additionally, there is a secondary peak following the main peak that does not appear in the other signals. One possible explanation is a higher refractive index creating a separation in the reflected peaks of air with tissue and tissue with slide

whereas generally these reflections are too close and overlap. Alternatively, there may be a physical separation between the tissue and the slide creating this secondary peak in signal B. This behavior of the measurement in the region of interest is even more pronounced in Sample 2, where the signal of point B in Fig. 13(b) occurs even earlier and the peaks are more pronounced.

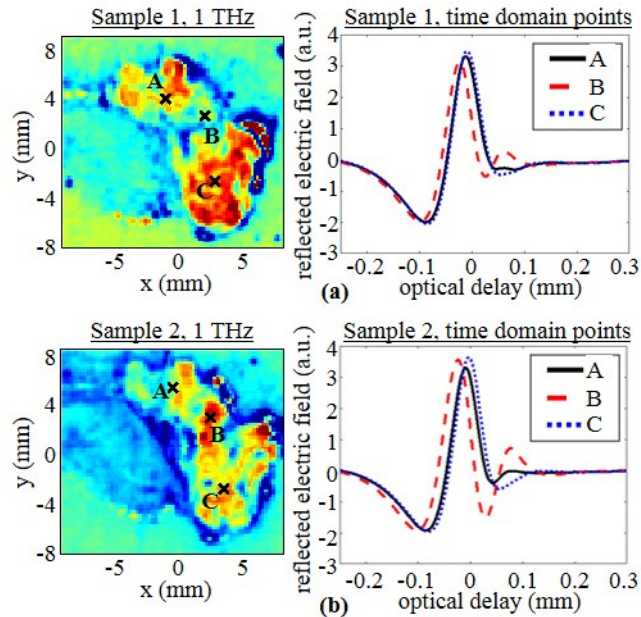


Fig. 13. Single point reflection comparison for three selected points A, B, C in lobular carcinoma scans for (a) Sample 1 and (b) Sample 2.

In order to determine whether the adhesion of the tissue to the slide is the problem in the selected samples, in depth images referred to as the B-scan are obtained across different lines on the imaging scan with the optical delay serving as the vertical axis as shown in Fig. 14. From this view of the imaging it is possible to note the areas where the tissue has separated from the polystyrene slide. The B-scan images of the two samples are shown in Fig. 14(a) for Sample 1 and in Fig. 14(b) for Sample 2. Here the scan of each section is observed using an  $x$ - $z$  axis cross-section taken at the indicated lines in the 1 THz frequency image of the reflection. In all B-scan images, the red interface indicates to the surface of the tissue with the air below. In looking at the B-scan images, Sample 1 only has two small noticeable spots where the surface of the tissue seems discontinuous in the third and fourth cross sections. However, these spots are at the far right edge of the lobular carcinoma where the separation of the tissue has also been observed in the time domain images of Fig. 10. For Sample 2 in Fig. 14(b), the B-scan images show relatively larger discontinuous spots in the first and second cross-sections. However, the separation observed in the first cross section occurs at the edge of the tissue. On the other hand, the second cross section shows potential separation of the tissue from the slide inside the carcinoma region. This corresponds to position 3 in the high power pathology in Fig. 12, where the collagenous tissue dominates, indicating to possible need for additional treatment of the sample prior to THz imaging.

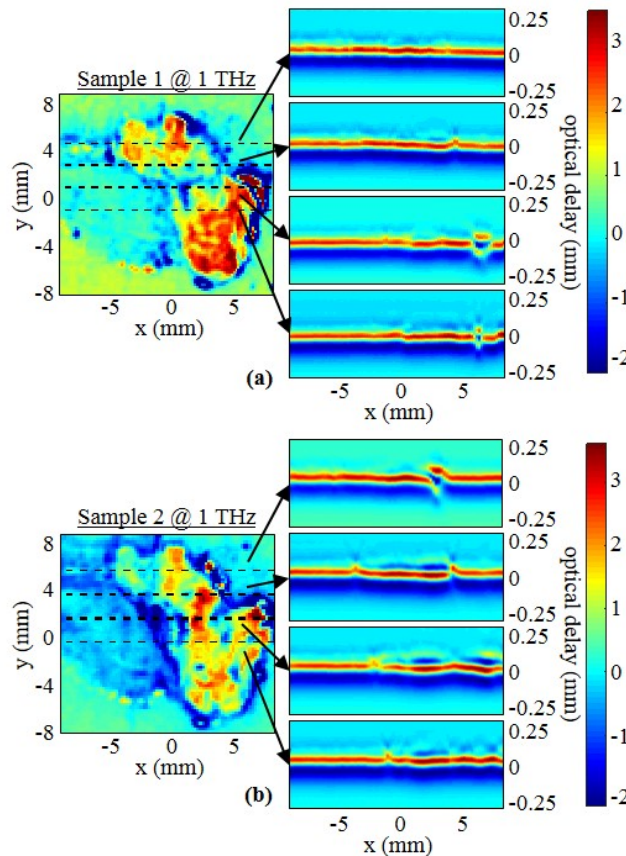


Fig. 14. B-scan reflection imaging used to investigate tissue adhesion to polystyrene slides for (a) Sample 1 and (b) Sample 2 of lobular carcinoma. Color bars indicate electric fields in B-scan images on the right in arbitrary unit (a.u.).

### 5.1.2 Calculation of refractive index and absorption coefficient of LC

The absorption coefficient and refractive index of the lobular carcinoma samples are calculated for Sample 1 using three tissue experimental setups: the transmission in Fig. 3, the reflection in Fig. 4(a) where the THz incident signal interacts with the tissue first, and the reflection in Fig. 4(b) where the THz signal interacts with the polystyrene slide first. All images in Fig. 15 are obtained at 1 THz. Figure 15(a) and 15(b) show the results based on solving Eqs. (3) and (4), the refractive index and absorption coefficient using the transmission setup. The results in Figs. 15(c)-15(d) and Figs. 15(e)-15(f) show the solution of Eqs. (8) and (9) using the setups in Fig. 4(a) and Fig. 4(b), respectively.

In order to solve for the properties of the lobular carcinoma using transmission, special consideration has to be taken for the nonuniform thickness of the polystyrene slide. This varying thickness across the slide, although in microns, causes a non-negligible phase variation in the measured signal that overwhelms the smaller phase differences from different tissue regions on the 30  $\mu\text{m}$  tissue. In order to account for this artifact phase, the thickness of the polystyrene outside of the tissue is estimated using the phase shift in the polystyrene alone (without tissue) and is interpolated beneath the tissue. The solved refractive index in Fig. 15(a) shows consistently higher values in the lobular carcinoma than in the healthy tissue. The absorption coefficient in Fig. 15(b) shows expected low values in the lobular carcinoma and fibroglandular tissue regions due to the lack of water in the tissue while the absorption coefficient in the fatty/fibroglandular mixed tissue region is shown to be insignificant.

The solution of the refractive index using the first reflection orientation in Fig. 15(c) demonstrates the sensitivity of the solution to the reflection phase. In this instance the solved refractive index shifts from high values in the upper right to lower values on the bottom left of the image due to variations in the slide surface thickness. While the variation in phase in the transmission mode could be estimated and accounted for, the reflection mode is significantly more sensitive to this phase variation as shown in Fig. 15(c) compared with 15a. As a result, the absorption coefficient solution in Fig. 15(d) is also poor in this case. The solution in Fig. 15(e) using the second reflection setup in Fig. 4(b) shows better images compared with Figs. 15(c)-15(d). However, the solution of the absorption coefficient in Fig. 15(f) shows the same issue as Figs. 15(b) and 15(d). Similar results are obtained using Sample 2 in addition to using the sandwiched setup in Fig. 4(c) (not shown here). It should be noted that there are no reported properties of lobular carcinoma in this frequency range for either fresh or FFPE tissue to compare with.

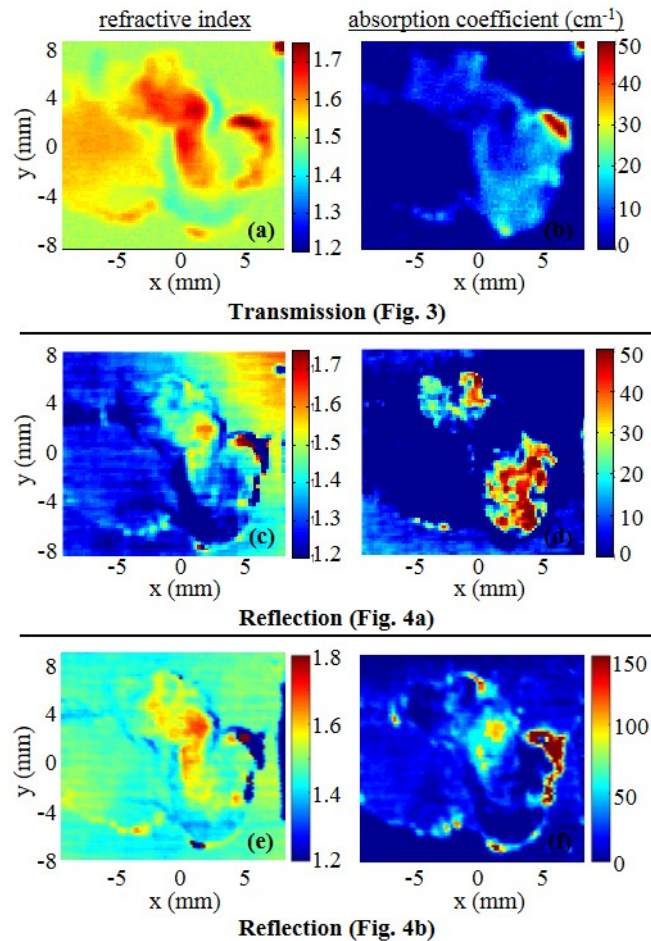


Fig. 15. Comparison between transmission and reflection solutions for Sample 1 of lobular carcinoma using (a),(b) transmission imaging following configuration in Fig. 3, (c),(d) reflection imaging with tissue facing the incident signal following configuration in Fig. 4(a), and (e),(f) reflection imaging with the polystyrene slide facing the incident signal following configuration in Fig. 4(b). All frequency images are at 1 THz.

While the THz reflection and transmission images in Figs. 10 and 11 clearly demonstrate the contrast between lobular carcinoma and fibroglandular tissue regions in both time and frequency domains, the calculated solution images in Fig. 15 lack clear boundaries between

the two regions, especially in the absorption coefficient images. These poor results of the refractive index and absorption coefficients could be explained by the insufficient thickness of the tested tissue. It should be noted that the work published in [11] for THz imaging of dehydrated liver cancer tissue used slices of 200  $\mu\text{m}$  thickness, and the work in [17] for THz imaging of freshly sliced breast tumors used 500  $\mu\text{m}$  thickness. While the 30  $\mu\text{m}$  tissue used in this work is sliced at the histology lab of NWA Pathology Associates using standard microtome, it is not a typical histopathology routine and has caused challenges in adhesion with the polystyrene slides as shown in Fig. 14. Slicing even thicker sections requires special equipment and special treatment of the slides to resolve the adhesion problem. Possible use of a vibratome for slicing thicker tissue up to 500  $\mu\text{m}$  will be used in future work in addition to treating the slides with poly-l-lysine and ozone activation.

## 5.2 Case 2: infiltrating ductal carcinoma (IDC)

### 5.2.1 Transmission and reflection images of IDC

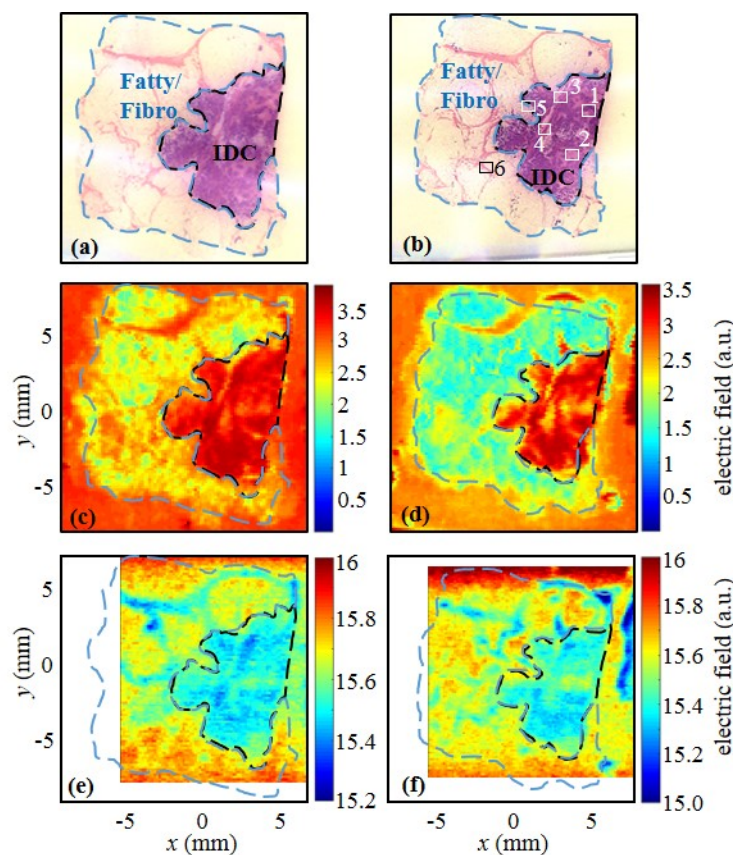


Fig. 16. Reflection and Transmission images of infiltrating ductal carcinoma samples obtained from 39-year-old woman. Pathology of (a) Sample 1 and (b) Sample 2 with regions designated by outlines for infiltrating ductal carcinoma (black) and fatty/fibroglandular (blue) tissue. Points 1-6 are indicated for high power pathology assessment to be shown in Fig. 18. Reflection peak time domain images are shown for (c) Sample 1 and (d) Sample 2. Transmission peak time domain images are shown for (e) Sample 1 and (d) Sample 2. Blank areas in the transmission images (e-f) represent the smaller scanning ranges (window size) in the transmission module in the measurement system used in this work, which is not the case for the reflection module in the system.

Additional THz imaging was applied to 20 and 30  $\mu\text{m}$  sections of the infiltrating ductal carcinoma (IDC) sample mounted on polystyrene slides. As with the sections of lobular

carcinoma, 5  $\mu\text{m}$  thick H&E stained slides were taken between each thick section. The histopathology and THz imaging results are shown in Fig. 16. Figure 16(a) shows the pathology image of Sample 1, which corresponds to a 20  $\mu\text{m}$  thick section, and Fig. 16(b) shows the pathology image of Sample 2 corresponding to a 30  $\mu\text{m}$  section. The H&E slides are highly similar and indicate the IDC region with dark purple stain on the right, while the clear or pink stain on the left indicates healthy fatty/fibroglandular tissue. The more defined pink traces show areas of dense, fibrous collagen in the fatty tissue. It should be noted that the images of Fig. 16 are smaller than that of Fig. 10 due to the IDC sample being 2 cm  $\times$  2 cm compared to the 1.5 cm  $\times$  2.5 cm of the lobular carcinoma. Several points designated 1-6 are selected in the histopathology of Section 2 shown in Fig. 16(b) for more detailed examination later in Fig. 18.

The time domain THz imaging of the samples in reflection mode can be seen in Fig. 16(c) for Sample 1 and Fig. 16(d) for Sample 2. As with the lobular carcinoma in Fig. 10, the carcinoma region in the pathology corresponds to a notably stronger reflection in the THz image. The contrast between the IDC and surrounding fatty/fibroglandular tissue is more apparent in the 30  $\mu\text{m}$  section in Fig. 16(d) compared to the 20  $\mu\text{m}$  section in Fig. 16(c), showing the improvement of the THz imaging as the thickness increases. THz imaging in the transmission mode is shown in Fig. 16(e) for Sample 1 and in Fig. 16(f) for Sample 2. Here the tissue shows lower transmission for the IDC compared to healthy tissue in agreement with the lobular carcinoma in Figs. 10(e) and 10(f), although it lacks details apparent in the reflection imaging in Figs. 16(c) and 16(d).

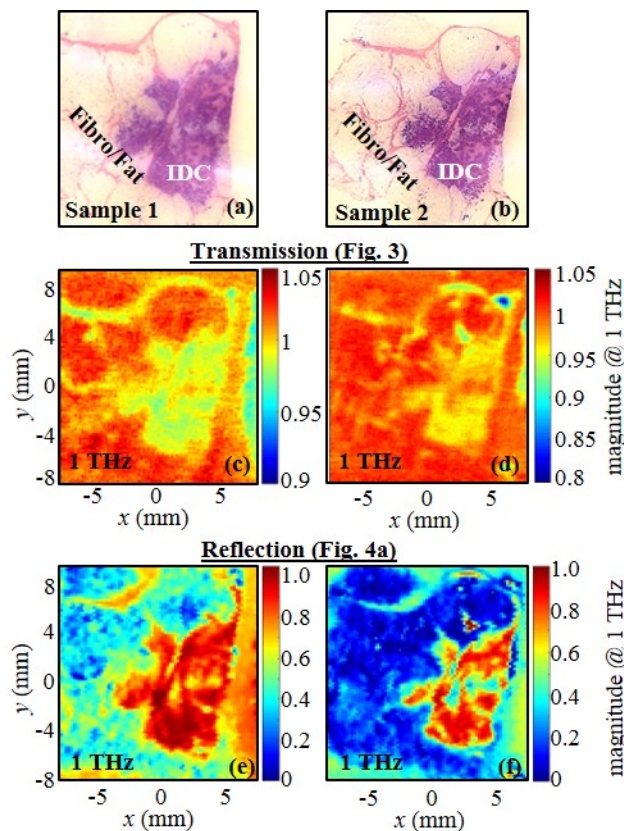


Fig. 17. Frequency domain images of infiltrating ductal carcinoma. Pathology given for (a) Sample 1 and (b) Sample 2. Transmission magnitude images at 1 THz for (c) Sample 1 and (d) Sample 2 following the configuration in Fig. 3 and reflection magnitude images at 1 THz for (e) Sample 1 and (f) Sample 2 following the configuration in Fig. 4(a).

Frequency domain images of the IDC sections are shown in Fig. 17. Unlike Fig. 11, only 1 THz images are shown here due to high frequency noise arising from multiple reflections in the slides used for these sections. Following the histopathology images in Figs. 17(a) and 17(b), the 1 THz transmission image is shown for Sample 1 in Fig. 17(c) and Sample 2 in Fig. 17d. The region of IDC can be seen more clearly than in the time-domain transmission images of Figs. 16(e) and 16(f) due to removing noise at higher frequencies. In particular, divisions in the IDC region become visible in the frequency domain in agreement with the pathology.

The transmission results show good consistency with the transmission through the lobular carcinoma in Figs. 11(c)-11(f). THz reflection images in Figs. 17(e) and Fig. 17(f) also show improved detail of the cancer edge as well as revealing interior details of the IDC region that can be seen in the pathology slides. The improved contrast and notable higher reflection is consistent with the lobular carcinoma in Figs. 11(g)-11(j).

In order to further examine the details of the interior of the IDC, high power pathology images were taken at the points indicated in Fig. 16(b). The resulting 100X magnification images are shown in Fig. 18. Here the primary IDC region consists of the dark purple stained epithelial cancer cells seen in the top half of position 1. Pink streaks in the middle of the cancer indicate fibrous desmoplasia induced by the cancer, indicating a scirrhous tumor. Larger regions of lighter staining like in position 2 indicate mostly fibrous regions on the interior of the tumor. One notable feature in the histopathology of Fig. 16(b) and in the frequency domain images of Fig. 17(f) is the large split in the IDC region. This can be seen in position 3 where a blood vessel surrounded by fibrous tissue in the center of the image divides the cancer in the lower right and fatty tissue in the upper left, and it is seen again in position 4 with the blood vessel in the lower right arising in the split, along with fatty tissue on both sides. While this split was not clear in the time domain images of Figs. 16(c) and 16(d), the 1 THz images in Fig. 17(f) show the separation in IDC regions clearly that can be attributed to the blood vessel and fat. The edge of the IDC with the surrounding fat tissue is shown in position 5, which is clear in all THz images in Figs. 16 and 17. Finally the pink regions in the fatty/fibrogladular tissue are mature collagen, seen in position 6 and shown in the time domain image of Fig. 16(d).

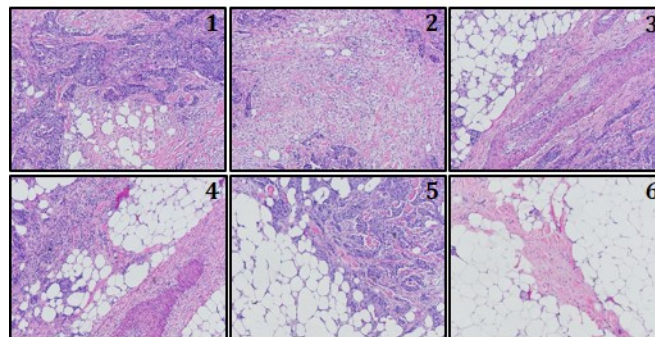


Fig. 18. High power pathology (100X) of positions 1-6 indicated in Fig. 16(b), showing neoplastic epithelial cells in position 1, interior fibrous tissue in position 2, blood vessels and fatty tissue dividing the IDC in positions 3-4, the edge of the epithelial cells with surrounding fat in position 5, and fibrous mature collagen in fatty tissue in position 6.

In the same manner that lobular carcinoma was examined for adhesion using the B-scan of the THz reflection image in Fig. 14, the two IDC samples are also investigated and presented in Fig. 19. For the 20  $\mu\text{m}$  section in Fig. 19(a), the B-scan shows relatively little change in the surface reflection at the cross-sections indicated by the black dashed lines. Thus Sample 1 can be seen to have good adhesion that is consistent across the entire tissue section. For the 30  $\mu\text{m}$  section in Fig. 19(b), the first cross-section shows a clear separation of the tissue in the center, along with a small separation at the edge of the tissue on the right side that extends into the second cross-section. Additionally, the fatty/fibrogladular tissue shows irregular reflections on the left side of all four cross-sections, but does not indicate any obvious separation of the

tissue from the slide. This is likely due to small variations in adhesion of fibrous tissue in the fatty/fibroglandular region, and it shows the difficulty in obtaining good adhesion in thicker sections as was already demonstrated for the lobular carcinoma in Fig. 14.

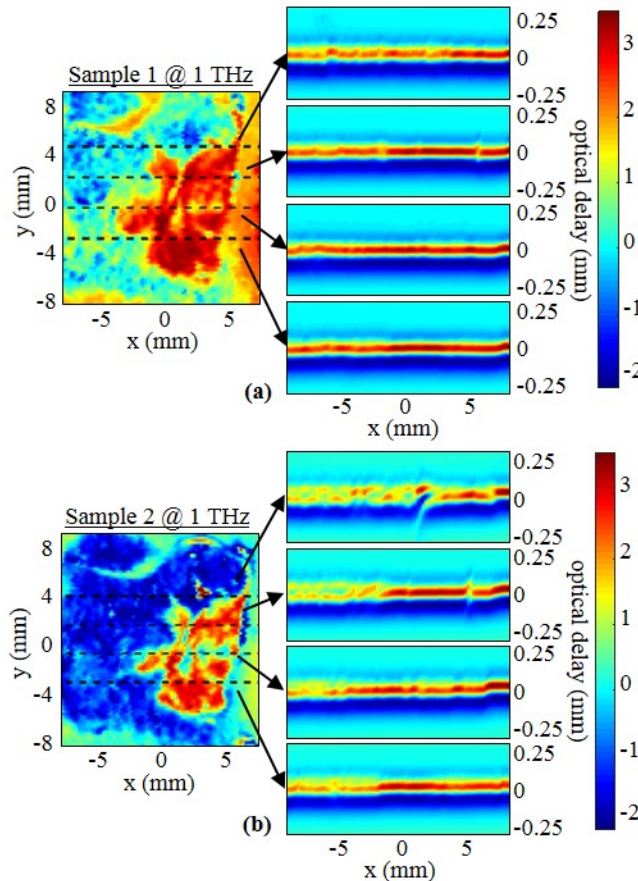


Fig. 19. B-scan reflection imaging used to investigate tissue adhesion to polystyrene slides for (a) Sample 1 and (b) Sample 2 of infiltrating ductal carcinoma. Color bars indicate electric fields in B-scan images on the right in arbitrary units (a.u.).

### 5.2.2 Calculation of refractive index and absorption coefficient of IDC

The absorption coefficient of the infiltrating ductal carcinoma samples are calculated for Sample 1 as shown in Fig. 20. The same experimental orientations of the tissue are used here similar to those used for the lobular carcinoma in Fig. 15. As observed in Figs. 15(a), 15(c), and 15(e), the refractive index solutions in the IDC case did not demonstrate the region of IDC as distinct from the fatty/fibroglandular tissue and are not presented here. This is likely due to inadequate tissue thickness and sensitivity to the polystyrene slide thickness that was often observed when the tissue thickness is comparable to the variation in slide thickness. The absorption coefficient solution shown in Figs. 20(a) and 20(b) seems to resolve the infiltrating ductal carcinoma, while the healthy tissue solution is too small to be fully resolved. This is consistent with the results seen in Figs. 15(b) and 15(d), where the lobular carcinoma is the only tissue region that resolves the absorption. Finally the absorption coefficient calculated from the reflection experimental measurements using the orientation of Fig. 4(b) in Fig. 20(c) demonstrates the IDC region much better than for the lobular carcinoma in Fig. 15(f). However, it is noteworthy that the solution is overexpressed in regions where the adhesion of

the tissue seen in the B-scan is in question in Fig. 14 for the lobular carcinoma and in Fig. 19 for the infiltrating ductal carcinoma. This is expressed in the center of the cancer in the lobular carcinoma in Figs. 15(f) and in the fatty/fibroglandular tissue of the infiltrating ductal carcinoma in Fig. 20(c).

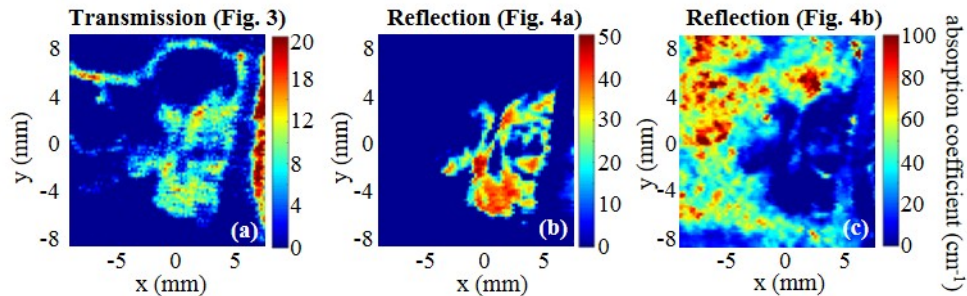


Fig. 20. Comparison between transmission and reflection solutions of the absorption coefficient for Sample 1 of infiltrating ductal carcinoma using (a) transmission imaging following configuration in Fig. 3, (b) reflection imaging with tissue facing the incident signal following configuration in Fig. 4(a), and (c) reflection imaging with the polystyrene slide facing the incident signal following configuration in Fig. 4(b). All frequency images are at 1 THz.

Overall the conclusion based on results of the infiltrating ductal carcinoma show strong agreement with the results already seen in the lobular carcinoma. The carcinoma in both cases shows strong contrast in the THz band against healthy tissue with higher reflection and more absorption in transmission mode. While the classification of the tissue remains subject to poor adhesion and sensitivity to slide thickness, THz imaging is shown to be effective for detecting the cancer even without the key contrast factor of the water content.

## 6. Discussion and conclusion

The results demonstrated that THz imaging is capable of clearly differentiating the margins of both lobular carcinoma and infiltrating ductal carcinoma from surrounding fibroglandular and fatty tissue for the dehydrated tissues used in this work. THz imaging in both transmission and reflection modes proved successful with some key differences between the two modes. Although transmission imaging show less image resolution due to possessing fewer focusing elements in the THz beam path, the calculation of tissue properties in transmission mode showed less sensitivity to tissue adhesion that can cause variation in phase. By comparison, the reflection imaging showed a higher imaging resolution and is a more suitable mode for imaging fresh tissue, as has been seen in skin cancer imaging [13]. Additionally, the increased resolution and sensitivity of the THz reflection imaging allowed for better differentiation of heterogeneous areas inside the carcinoma that compared well with high power pathology images. Reflection imaging has shown the ability to distinguish not just the carcinoma from healthy tissue, but also to show contrast between different densities of cancer cells.

Identifying the polarization of the THz beam in the reflection mode was a challenge due to the use of multiple parabolic mirrors to direct and focus the beam. However, modeling the polarization angle of the beam and comparing against experimental data led to a good estimation of the hybrid polarization of  $TE$  and  $TM$  modes. This hybridized polarization was successfully validated on fresh bovine tissue.

Numerical challenges are observed in calculating the refractive index and absorption coefficient in the FFPE tumor cases due to the small thickness of the tissue compared with the polystyrene slide. Basically, the dehydrated tissue is considered a weak scatterer compared to the slide used to support the tissue leading to poor solutions. These problems could be resolved using thicker tissue sections and slide treatment to enhance tissue adhesion in future work.

While the current work does not address breast cancer margin assessment directly, it does represent a step forward in the methodology for eventual application while addressing some of the practical challenges in determining the origin of tissue contrast. Implementing the above techniques on freshly excised breast tumors requires moving the technology to the hospital similar to the work by Fitzgerald *et al.* [18]. Implementing the THz techniques into future clinical practice will require more research and clinical trials.

### Appendix A

All modeling in this work is based on the impedance and reflection across a multiple layered system [34,35]. This results in a term based on reflection coefficients at the interfaces  $\rho_{ij}$  and propagation terms through each region in the form of  $\exp(-j2\frac{\omega}{c}\tilde{n}_1\cos\theta_1d_1)$ , where  $i$  and  $j$  represent the layers across the interface as seen in Eqs. (2) and (5). For the transmission mode the signal has a normal incidence  $\theta_i = 0$ , however, for oblique incidence at  $30^\circ$ , the reflection coefficients of each region rely on the polarization of the beam. In (5), where  $\Gamma_T$  uses the following expressions for the *TE* mode

$$\rho_{T,ij} = \rho_{TE,ij} = \frac{\tilde{n}_i \cos \theta_i - \tilde{n}_j \cos \theta_j}{\tilde{n}_i \cos \theta_i + \tilde{n}_j \cos \theta_j}, \quad (10)$$

and the following expression for the *TM* mode

$$\rho_{T,ij} = \rho_{TM,ij} = \frac{\tilde{n}_i \cos \theta_j - \tilde{n}_j \cos \theta_i}{\tilde{n}_i \cos \theta_j + \tilde{n}_j \cos \theta_i}. \quad (11)$$

### Funding

National Science Foundation (NSF) (MRI 1228958, 1408007, DGE-1450079); University of Arkansas DDF.

### Acknowledgments

The Authors would like to thank the staff at Northwest Arkansas Pathology Associates, P.A., for providing tissue and histopathology services for the carcinoma. The Authors would also like to thank Dr. Keith Bailey, Clinical Associate Professor and Comparative Pathologist at Oklahoma State University, for additional pathology assessment.